The biochemical composition of the actomyosin network sets the magnitude of cellular traction forces

Somanna Kollimada, Fabrice Senger, Timothée Vignaud, Manuel Théry, Laurent Blanchoin, Laëtitia Kurzawa

The biochemical composition of the actomyosin network sets the magnitude of cellular traction forces

Somanna Kollimada[a], Fabrice Senger[a], Timothée Vignaud[a,b], Manuel Théry[a,c,*], Laurent Blanchoin[a,c,*], and Laëtitia Kurzawa[a,*]

[a]Interdisciplinary Research Institute of Grenoble, Laboratoire de Physiologie Cellulaire & Végétale, CytoMorpho Lab, University of Grenoble-Alpes, CEA, CNRS, INRA, Grenoble, France; [b]Clinique de chirurgie digestive et endocrinienne, Hôtel Dieu, Nantes, 44093, France; [c]Institut de Recherche Saint Louis, U976 Human Immunology Pathophysiology Immunotherapy (HIPI), CytoMorpho Lab, University of Paris, INSERM, CEA, Paris, France

ABSTRACT **The regulation of cellular force production relies on the complex interplay between a well-conserved set of proteins of the cytoskeleton: actin, myosin, and α-actinin. Despite our deep knowledge of the role of these proteins in force production at the molecular scale, our understanding of the biochemical regulation of the magnitude of traction forces generated at the entire-cell level has been limited, notably by the technical challenge of measuring traction forces and the endogenous biochemical composition in the same cell. In this study, we developed an alternative Traction-Force Microscopy (TFM) assay, which used a combination of hydrogel micropatterning to define cell adhesion and shape and an intermediate fixation/immunolabeling step to characterize strain energies and the endogenous protein contents in single epithelial cells. Our results demonstrated that both the signal intensity and the area of the Focal Adhesion (FA)–associated protein vinculin showed a strong positive correlation with strain energy in mature FAs. Individual contents from actin filament and phospho-myosin displayed broader deviation in their linear relationship to strain energies. Instead, our quantitative analyzes demonstrated that their relative amount exhibited an optimum ratio of phospho-myosin to actin, allowing maximum force production by cells. By contrast, although no correlation was identified between individual α-actinin content and strain energy, the ratio of α-actinin to actin filaments was inversely related to strain energy. Hence, our results suggest that, in the cellular model studied, traction-force magnitude is dictated by the relative numbers of molecular motors and cross-linkers per actin filament, rather than the amounts of an individual component in the cytoskeletal network. This assay offers new perspectives to study in more detail the complex interplay between the endogenous biochemical composition of individual cells and the force they produce.**

Monitoring Editor
Alexander Dunn
Stanford University

Received: Mar 8, 2021
Revised: May 3, 2021
Accepted: May 11, 2021

This article was published online ahead of print in MBoC in Press (http://www.molbiolcell.org/cgi/doi/10.1091/mbc.E21-03-0109).

Competing Interests: The authors declare no competing financial or other interests.

*Address correspondence to: Laëtitia Kurzawa (laetitia.KURZAWA@cea.fr); Laurent Blanchoin (laurent.blanchoin@cea.fr); Manuel Théry (manuel.thery@cea.fr).

Abbreviations used: ECM, Extracellular Matrix; FA, Focal Adhesion; FAAS, Focal Adhesion Analysis Server; p-MLC, phospho-Myosin Light Chain; RPE-1, Retinal Pigment Epithelial-1; TFM, Traction Force Microscopy.

INTRODUCTION

Mechanical forces are central to many physiological processes, including morphogenesis (Heisenberg and Bellaïche, 2013; Murrell *et al.*, 2015), migration (Maiuri *et al.*, 2015; Leal-Egaña *et al.*, 2017), division (Sedzinski *et al.*, 2011), and differentiation (McBeath *et al.*, 2004; Kilian *et al.*, 2010). All these events involve tight regulation of both the magnitude and the spatial distribution of the contractile forces at the levels of the cell and tissue (Murrell *et al.*, 2015; Agarwal and Zaidel-Bar, 2019).

At the macromolecular level, the tight regulation of cellular force depends on key parameters including substrate stiffness (Lo *et al.*, 2000), adhesive-ligand density (Reinhart-King *et al.*, 2005), cell area

(Califano and Reinhart-King, 2010), and shape (Rape *et al*., 2011). At the molecular level, the regulation of force production and transmission relies on a complex interplay between a well-conserved set of proteins of the cytoskeleton. In essence, force originates from the interactions between actin filaments and non-muscle myosin II (Chrzanowska-wodnicka and Burridge, 1996; Katoh *et al*., 1998; Koenderink and Paluch, 2018). Indeed, the initial generation and magnitude of traction force by these actomyosin structures are determined by the amount of active myosin and the local alignment and connectivity of actin filaments (Bendix *et al*., 2008; Thoresen *et al*., 2011; Reymann *et al*., 2012; Luo *et al*., 2013; Ennomani *et al*., 2016; Linsmeier *et al*., 2016). Hence, the remodeling of actin filament by the action of cross-linkers, in particular of α-actinins, plays a key role in regulating the mechanical properties of the network (Xu *et al*., 1998) and can give rise to the formation of stress fibers (Lazarides and Burridge, 1975; Langanger *et al*., 1986). Such stress fibers are essential for tension generation against the extracellular matrix (ECM), via focal adhesion (FA) complexes, and propagate contractile forces throughout the cell (Deguchi *et al*., 2005; Naumanen *et al*., 2008; Chang and Kumar, 2013). In turn, the degree of contractile force transmitted to the cell surroundings depends on the composition, size and dynamics of FA complexes (Elosegui-Artola *et al*., 2016).

However, it remains less clear how the magnitude of the traction force is regulated by the numerous different proteins and the interplay between these proteins in the actomyosin networks and cell adhesion complexes. Although the role of this set of proteins in force regulation appears to be well conserved (Murrell *et al*., 2015), the relative amount, biochemical state, and structural organization can vary locally within a cell and more globally between cells, thus affecting the magnitude of cellular traction force (Kurzawa *et al*., 2017). This lack of clarity is notably reflected in the relationship between force and the characteristics of the FA, which remains controversial, as observations made in migrating cells or in cells overexpressing adhesion proteins have not been reproduced in other cellular contexts. Thus, FA size and force were shown to be correlated only during the initial steps of the FA maturation process (Stricker *et al*., 2011). The linear relationship described between the size of individual adhesions above 1 μm^2 and the amount of local force (Balaban *et al*., 2001) does not hold when supermature FAs above 8 μm^2 (Goffin *et al*., 2006) or smaller FAs, in which the stress is highly variable (Tan *et al*., 2003), are considered. Moreover, a counterintuitive relationship was described in migrating cells, in which small FAs at the leading edge were associated with strong forces, in contrast to larger FAs at the trailing edge being associated with weaker forces (Beningo *et al*., 2001).

Traction force microscopy (TFM), a method that maps the force at the cell surface by measuring deformations of the underlying substrate, greatly helped in identifying the molecular components involved in force production and regulation (Dembo and Wang, 1999; Kraning-Rush *et al*., 2011). However, despite its extensive use, this straightforward technique includes a disruptive step of cell removal, precluding further characterization of the biochemical composition of the cellular network responsible for the production of traction force. In the case of FAs in particular, the characterization of their molecular morphometry has been limited to live observations of fluorescent proteins fused to paxillin or vinculin, thereby preventing the assessment of endogenous levels of these proteins (Balaban *et al*., 2001; Möhl *et al*., 2012; Plotnikov *et al*., 2012). Other methods, including 2D micropillars (Tan *et al*., 2003; Biais *et al*., 2012), DNA-based sensors (Grashoff *et al*., 2010), and reference-free techniques (Bergert *et al*., 2016; Banda *et al*., 2019), provide alternative ways to measure intracellular forces without requiring cell detachment and therefore permit further cell characterization. However, these other methods also have intrinsic limitations (Roca-Cusachs *et al*., 2017). Micropillars interfere with cell behavior due to the non-continuous nature of the pillars, their topography, and the fact that cell adhesions are geometrically constrained (Trichet *et al*., 2012; Bergert *et al*., 2016; Griffin *et al*., 2019). DNA force-based sensors can measure precisely the maximal force produced by cells, but not the lower values, and in addition, do not provide information about force directionality (Wang and Ha, 2013). Global or local deformations of micropatterned cells are not precise enough to investigate the finer aspects of how traction force is regulated (Tseng *et al*., 2011; Pushkarsky *et al*., 2018; Ghagre *et al*., 2021). Hence, alternative methods are required to evaluate the relationship between traction force and the biochemical composition of the cytoskeletal network in the same cell.

To evaluate how the traction force exerted by a cell is related to the biochemical composition of its cytoskeletal networks, we have developed an alternative TFM method. In this method, epithelial cells were grown on a micropatterned substrate to normalize cell shape and size and a fixation and an immunolabeling step were included before the cell detachment required for traction force computation. This method enabled us to study the relationship between strain energy, as a readout of force exerted by these cells on their substrates, and the amounts of vinculin, F-actin, phospho-myosin, and α-actinin at the level of the entire cells. In this cellular context, our results identified a strong positive correlation between strain energy and the total area and signal intensities of vinculin present in mature FAs. In contrast to vinculin, actin and phospho-myosin individual content displayed broader deviations in their linear relationship to the strain energies, and thus appear as less straightforward and reliable predictors of force. Instead, our data suggested that the relative content of phospho-myosin per actin exhibited an intermediate and optimum ratio maximizing the production of force by the cells. Finally, although no correlation was identified between strain energy and the individual amount of α-actinin, strain energy was inversely related to the ratios of α-actinin to F-actin and phospho-myosin.

RESULTS

Development of a modified traction force microscopy assay

To study how the intrinsic composition of the cytoskeletal network relates to the traction force exerted by cells on their substrates, we adapted the conventional TFM assay and focused on a set of proteins involved in intracellular force generation and transmission: vinculin, actin filament, phospho-myosin, and α-actinin.

In the standard TFM assay, traction forces are calculated from the displacement of an array of fluorescent beads in a deformable substrate: the positions of the beads are imaged first when the cell is attached to and deforms the gel (Figure 1A, Step 1) and then after the cell is removed by trypsinization and the gel is in relaxed configuration (Figure 1A, Step 2). In our adapted assay after Step 1, the cell was imaged after being fixed and stained with fluorescently labeled antibodies (Figure 1B). The cell was then removed, and the traction forces were calculated by bead displacement from Step 1, as we noticed that the fixation procedure led to a significant but not full relaxation of the gel (Supplemental Figure 1A).

The cytoskeleton molecular composition and organization can vary drastically from one cell to another, and as both parameters are intimately linked to the force generation process, studying how they relate to each other turns out to be challenging in a heterogeneous cell population. We therefore plated human retinal pigment epithelial-1 (RPE-1) cells on soft dumbbell-shaped micropatterns

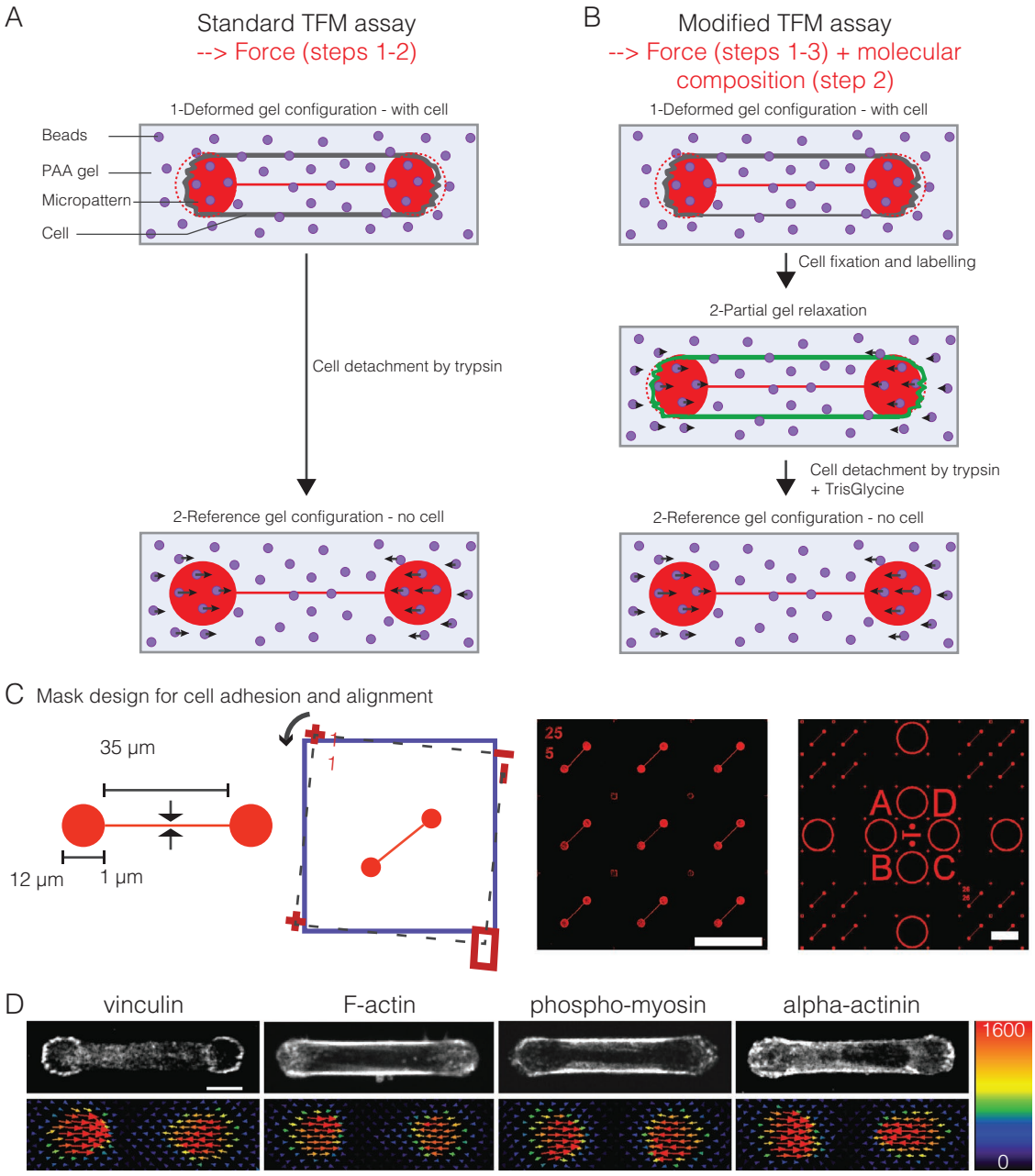

FIGURE 1: Development of a modified TFM assay including a fixation and labeling step enabling the concomitant traction force measurement and intracellular composition analysis. (A) Scheme displaying the two steps of a standard TFM assay. (B) Scheme of the modified TFM assay including an intermediate fixation and immunolabeling step of the cells. (C) Left panel: scheme of the dumbbell-shaped micropattern and its associated dimensions. Middle panel: representation of the micropattern in a field of view used for imaging and of the fiduciary marks in the corners used for the rotation correction. Right panels: representative low-magnification images of the dumbbell shaped micropatterns and fiduciary marks (Fibrinogen-cy3) used for retrieving the exact sample position between the different steps of the TFM process. Image scale bars = 100 µm. (D) Selected images of RPE-1 cells immunostained for vinculin, F-actin (phalloidin), p-MLC, α-actinin 4, and the associated traction stress maps computed in the same cells. Image scale bar = 10 µm. Force scale color bar in Pa.

coated with fibronectin to minimize this inherent variability (Figure 1C). The micropattern length of 59 µm was selected because it corresponds to the average length of the RPE-1 cell (Vignaud *et al.*, 2021). Reference marks were also included in proximity to the micropatterns, to ensure the correct localization of individual cells through all of the steps of the TFM assay (Figure 1C), and to support a computational correction on the alignment of the beads based on a cross-correlative approach at the end of the assay (Supplemental Figure 1B).

As previously described (Vignaud *et al.*, 2021), most cells were able to attach and spread fully on the fibronectin micropattern within 4 h (Supplemental Figure 2A). Cells not fully spread on the micropattern or extending their protrusions outside of the micropatterned area were excluded from the analysis (Supplemental Figure 2B). As

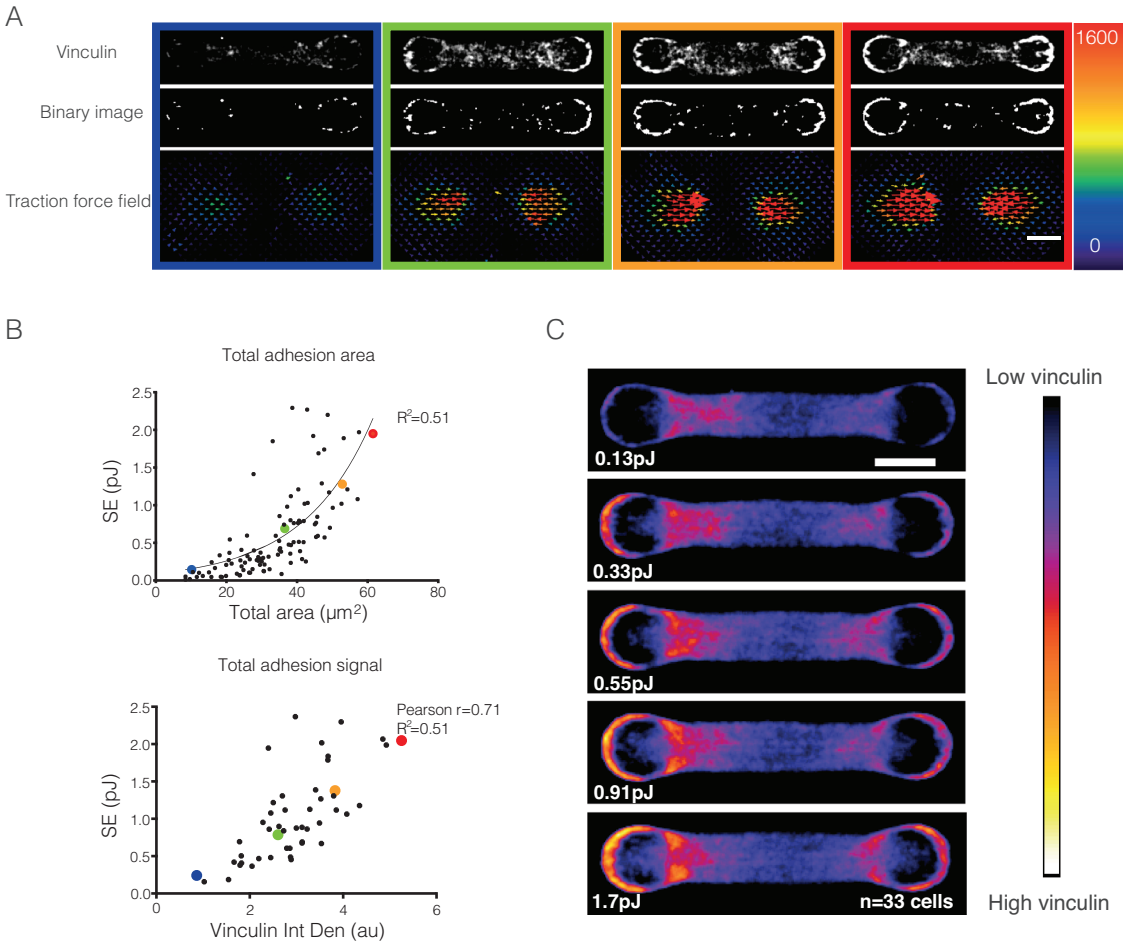

FIGURE 2: Total cellular vinculin content and area represent good predictors of cell strain energy. (A) From top to bottom: images of RPE-1 cells labeled for vinculin; corresponding binary images obtained following image thresholding by intensity; associated traction stress maps. Image scale bar = 10 μm. Force scale color bar in Pa. (B) Top panel: scatter plot of the strain energy (pJ) as a function of total vinculin area (μm²). The R^2 corresponding to an exponential growth fit is indicated on top of the plot. Data were pooled from two independent experiments. Color-coded points following the trend of an exponential regression were selected and the corresponding cells and traction stress maps highlighted in Top panel with the same colors. Bottom panel: scatter plot of the strain energy (pJ) as a function of total vinculin signal intensity (au). The Pearson correlation coefficients and corresponding R^2 are indicated on top of the plot. $N = 1$ experiment. (C) From top to bottom: representation of averaged intensity projections of vinculin immunostainings from cells displaying increasing strain energy ($n = 33$ cells for each image). Averaged strain energy values for each group is indicated at the bottom left of the image. Image scale bar = 10 μm.

expected (Vignaud *et al.*, 2021), the FA protein vinculin was mainly localized in the cell above the two main adhesive areas of the micropattern (Figure 1D). Additionally, two peripheral prominent stress fibers containing actin, phospho-myosin, and α-actinin spanned the non-adhesive area between these adhesion points (Figure 1D). The strain energies ranged from 0 to 2.5 pJ, as previously described for the same experimental conditions using the conventional TFM method (Vignaud *et al.*, 2021).

These results show that, even with partial relaxation of the gel during fixation and the sample repositioning step after the immunolabeling, strain energy and the molecular composition of the cytoskeleton can be measured in the same cell, thereby validating our experimental approach.

Correlation between focal adhesion area, vinculin content, and force in mature focal adhesion

The modified TFM assay was first used to investigate the controversial relationship between cell strain energy and FA complexes, using vinculin as a marker, because it is found in both focal complexes (DePasquale and Izzard, 1987) and larger and more stable FAs (Geiger *et al.*, 2001). Given that the cells were plated on the micropatterns several hours before the TFM assay, the FAs were considered to be fully mature and not subject to turnover, as would be found in motile cells. Key FA parameters, the overall size of the areas of positive vinculin staining (vinculin adhesion area) and the overall signal intensity of vinculin staining, were captured and processed using Focal Adhesion Analysis Server (FAAS) (Figure 2A; see *Materials and Methods*). The entire cell was selected for the FA analysis because we have previously shown that traction forces applied to the ECM at anchorage points were generated not only by prominent stress fibers, but also by actin mesh in which these structures are embedded (Vignaud *et al.*, 2021).

Interestingly, although cell shapes were standardized by the micropattern substrate, the total vinculin adhesion areas and total vinculin signal intensities displayed large variations between cells (Figure 2, A and B). The associated strain energies also exhibited a

large heterogeneity among the cells analyzed. We first observed that total vinculin adhesion area was related to strain energy, so that strain energy increased exponentially with the increase in vinculin adhesion area (Figure 2, A and B, Top panel; $R^2 = 0.51$). In addition, vinculin signal intensity was positively correlated to strain energy (Figure 2, A and B, Bottom panel; Pearson = 0.71; $R^2 = 0.51$). These results indicate that both total vinculin adhesion area and signal intensity are good predictors of the magnitude of traction force in stationary cells. Moreover, the vinculin signal was not uniformly intense throughout the adhesive area of the micropattern but was mainly confined to the periphery of the cell in areas corresponding to the lamellum region (Figure 2C). With greater strain energies, this adhesion pattern formed beltlike structures of increasing length, but not thickness, above the circumference of each of the two circular parts of the micropattern. Hence, these results suggest the existence of a mechanism limiting the extension of FA toward the more internal part of the cell.

Correlation between strain energy and total or stress fiber–related F-actin content

We next tested whether the heterogeneity in the magnitude of traction forces observed was associated with actin filament content. The relationship between actin filament and traction force was investigated using phalloidin-FITC staining (Figure 3). Actin filament content was measured throughout the cell (Figure 3A) and within the two stress fibers that formed at the periphery of the long edge of the cell between the adhesive areas (Figure 3B). As with vinculin, total actin filament content in the entire cell and within stress fibers varied between cells. Nevertheless, total cellular actin filament content was linearly related to strain energy (Pearson = 0.57, $R^2 = 0.32$; pink dots and box in Figure 3, A and C, respectively); and total actin filament content within stress fibers linearly increased with strain energy (Pearson's $r = 0.55$, with $R^2 = 0.30$). Unexpectedly, the correlation coefficients for actin filament content in the entire cell or within stress fibers were almost identical, showing that actin filament in stress fibers, that is, the structures dedicated to force production, did not represent a better predictor of force than the total cellular actin filament content.

Although correlated with force, the values for actin filament content in the entire cell or within stress fibers were dispersed around the linear trend in the correlations with strain energy (Figure 3, A and B). For example, cells displaying the same amounts of actin filament had a wide range of strain energies, from 0.2 to 1.4 pJ (green dots and box in Figure 3, A and C, respectively). Conversely, cells displaying the same strain energy had a wide range of actin filament content (orange dots and box in Figure 3, A and C, respectively). This suggested that actin filament content could only partially predict traction force magnitude, and therefore other factors were involved in traction force generation.

Correlation between strain energy, phospho-myosin, and actomyosin content

The relationship between the motor activity of myosin and traction force was investigated using phospho-myosin light-chain staining (phospho-myosin). The phospho-myosin signal in the entire cell varied between cells and was linearly related to strain energy (Pearson = 0.67, $R^2 = 0.45$; pink dots and box in Figure 4, A and B, respectively). The correlation coefficient was higher than that for total actin filament with strain energy, indicating that phospho-myosin represents a better predictor of traction force magnitude than F-actin. Nevertheless, cells displaying the same amount of phospho-myosin had a wide range of strain energies, and conversely, cells displaying the same strain energy had a wide range of phospho-myosin content (green and orange dots and boxes in Figure 4, A and B, respectively). Therefore, as with actin filament content, this suggested that phospho-myosin content could only partially predict traction force magnitude.

Given the weak correlations of actin filament and phospho-myosin content with strain energies, and the known functional interrelationship between actin filament and myosin, we then combined phospho-myosin staining with actin filament staining in the modified TFM assay. We postulated that traction forces might scale linearly with phospho-myosin and actin content, as more phospho-myosin in the actin network should increase the contractility. First, we observed that phospho-myosin content was linearly related to total F-actin content (Pearson = 0.71, $R^2 = 0.5$ in Figure 4C, left panel); and second, the linear relationships with strain energy were confirmed for both phospho-myosin content and actin filament content (as illustrated by the color-coded representation of the strain energy in between the two dashed lines; Figure 4C, left panel). Unexpectedly, we also observed that outside of this linear regime, forces dropped drastically (below 0.5 pJ) despite the presence of a large amount of either actin filaments or phospho-myosin. This suggested that the value of the actomyosin was key to setting the magnitude of traction forces exerted by cells, so we next decided to plot the ratio of phospho-myosin to actin filaments versus strain energy (Figure 4C, right panel). The ratio of phospho-myosin to actin filament content displayed no correlation with strain energy (Pearson = -0.006, $R^2 = 3.38 \times 10^{-5}$). More interestingly, an intermediate and optimum ratio (in between the two dashed lines) was required for cells to produce high forces (defined as above 1 pJ). For low phospho-myosin/actin filament ratios, corresponding to the case where the proportion of actin filaments to phospho-myosin was higher than the averaged trend, the forces measured were below 0.5 pJ. The opposite trend appeared deleterious as well: when phospho-myosin/actin filament ratio was higher than the average, cells were limited to the same low range of force. These results showed that although, when considered individually, larger amounts of actin or phospho-myosin correspond to higher force, an optimal balance between total amount of phospho-myosin and actin filament exists and leads to maximization of the production and transmission of traction forces.

Correlation between strain energy, α-actinin content, and α-actinin/F-actin and α-actinin/phospho-myosin ratios

Unlike the other evaluated contractile-network proteins, no correlation was identified between α-actinin content in the entire cell and strain energy (Figure 5A; Pearson's $r = 0.08$, $R^2 = 0.007$), suggesting that the relative proportion of this cross-linker compared with the actin filament may be more meaningful. When α-actinin was considered together with actin filament in the same cells, α-actinin content was linearly related to actin filament content (Pearson $r = 0.59$, $R^2 = 0.35$ in Figure 5B, left panel). However, in contrast to the phospho-myosin/actin filament ratio, the strain energies appeared maximal when the ratio of α-actinin to actin filament content was low. To explore further the relationship between α-actinin and actin filament relative content, we next plotted the strain energy as a function of the ratio of these protein contents (Figure 5B, right). We observed that the increase in α-actinin to actin filament ratios was associated with an exponential decay of force ($R^2 = 0.48$). This result indicated that for high α-actinin/actin filament ratios, meaning that α-actinin levels were high for a given amount of actin filament, the transmission of force to the substrate was limited to a low range of force, below

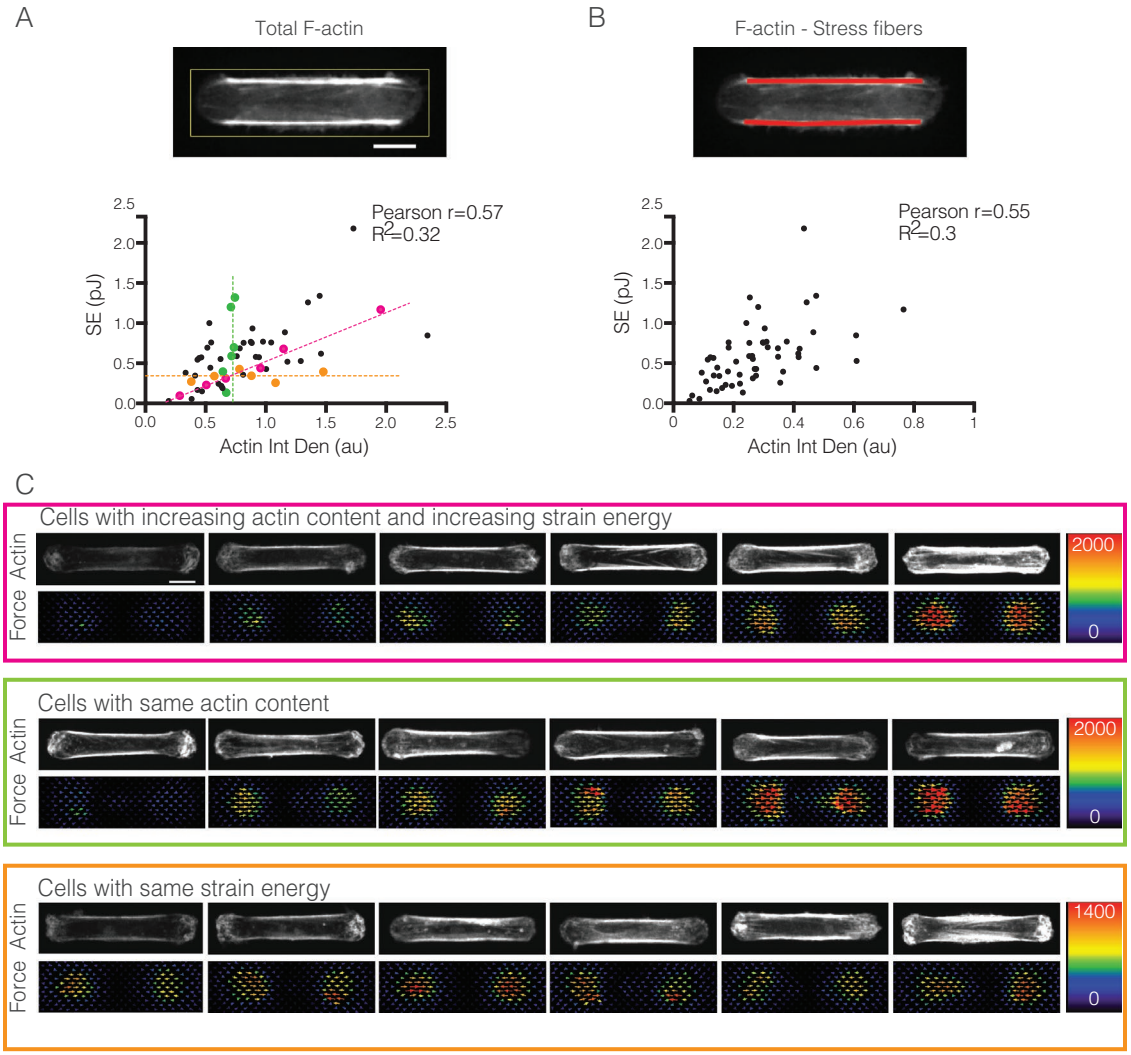

FIGURE 3: Total actin filament and SF-related actin filament contents display linear increase with force but exhibit broad variations from this trend. (A) Top panel: image of an RPE-1 cell depicting the area used for measurement of total F-actin signal (yellow box). Image scale bar = 10 µm. Bottom panel: scatter plot of the strain energy (pJ) as a function of total actin signal (au). The Pearson correlation coefficient and corresponding R^2 are indicated on top of the plot. Different color-coded points were selected on the plot and the corresponding cells and traction stress maps are highlighted in the images in C. Pink indicates cells following a linear regression; orange: cells exerting the same level of strain energy but displaying high variability in actin content; green: cells displaying the same actin content but high variability in strain energies. (B) Top panel: image of an RPE-1 cell depicting the area used for measurement of F-actin signal integrated over the stress fibers (red lines). Image scale bar = 10 µm. Bottom panel: scatter plot of the strain energy (pJ) as a function of F-actin signal in peripheral stress fibers (au). The Pearson correlation coefficient and corresponding R^2 are indicated on top of the plot. (C) Top panels: images of RPE-1 cells labeled for actin (phalloidin). Bottom panels: corresponding traction stress maps. Image scale bar = 10 µm. Force scale color bar in Pa. The color-code of the boxes refers to the points highlighted in the scatter plot in A.

0.4 pJ (Figure 5B, right panel, and c). In contrast, high force production was limited to cells displaying low α-actinin ratios to actin filaments. Intriguingly, these results differed from the bell-shaped contractile response previously described for actin networks in vitro (Bendix *et al.*, 2008; Alvarado *et al.*, 2013; Ennomani *et al.*, 2016), as no force drop was registered at low actinin/actin filament ratios. Instead, they show that in cells, a low amount of cross-linker per actin filament is required to generate high forces.

To explore further the contribution of the couple phospho-myosin–α-actinin in relationship to force, we also studied the variation of both protein contents and their associated traction forces in the same cells (Supplemental Figure 3A). As in the case of the total α-actinin and actin filament content, but to a lesser extent, the total α-actinin and phospho-myosin content were positively correlated, reaching a plateau for intermediate to high α-actinin values (Pearson's $r = 0.37$; $R^2 = 0.14$). The strain energies also appeared maximal when the ratio of α-actinin to phosphomyosin was low. This was further illustrated when strain energy was plotted as a function of the ratio of the two protein contents (Supplemental Figure 3B), as we observed that the increase in the α-actinin/phospho-myosin ratio was accompanied by an exponential decay of force ($R^2 = 0.59$). These results altogether demonstrate that high force production is limited to cells displaying low α-actinin per F-actin and phospho-myosin content.

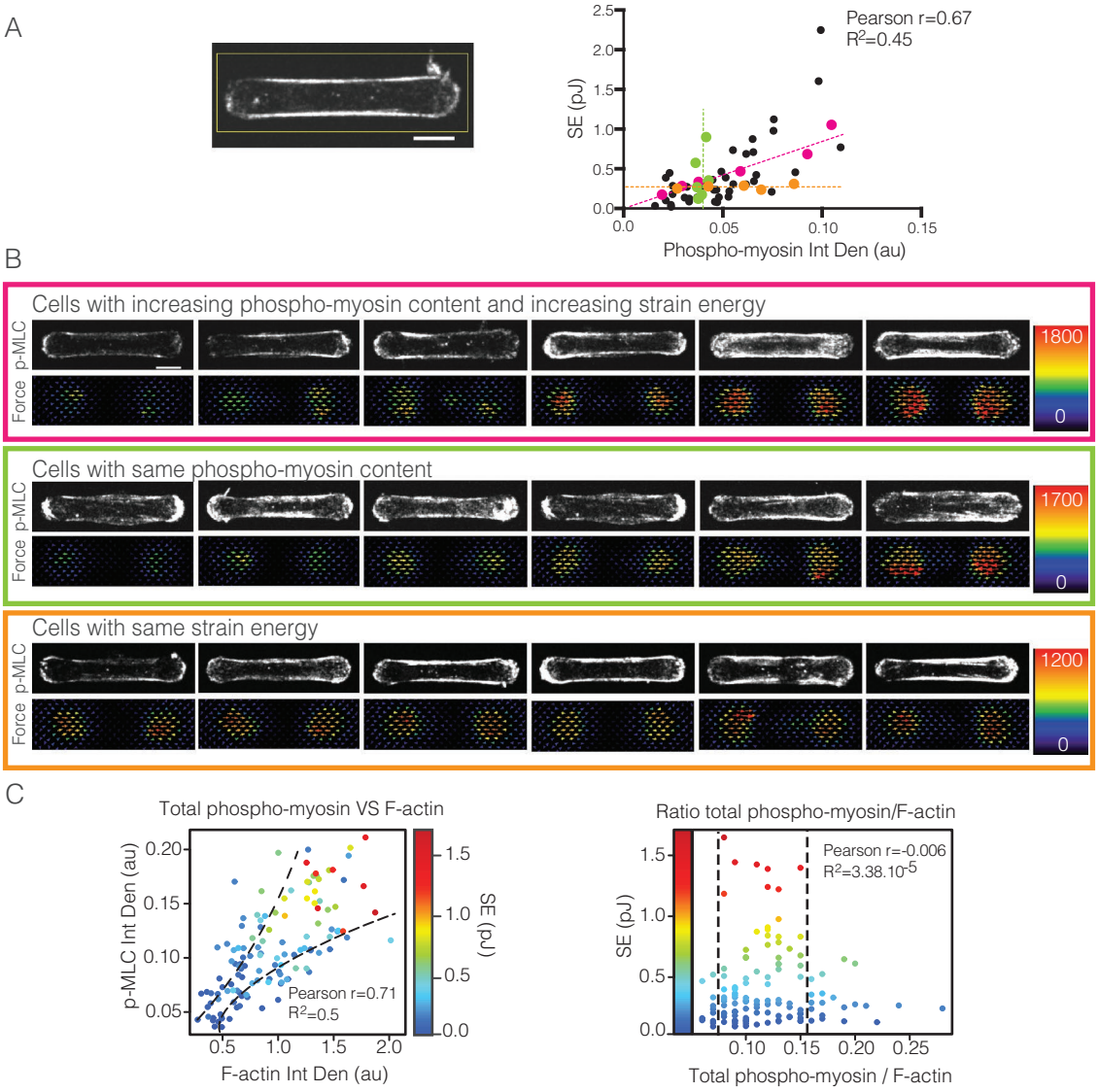

FIGURE 4: The actomyosin/actin filament ratio displays an optimal range allowing the maximal traction force production by cells. (A) Left panel: image of an RPE-1 cell depicting the area used for measurement of total phospho-myosin signal (yellow box). Image scale bar = 10 μm. Right panel: scatter plot of the strain energy (pJ) as a function of total phospho-myosin signal (au). The Pearson correlation coefficient and corresponding R^2 are indicated on top of the plot. Different color-coded points were selected on the plot and the corresponding cells and traction stress maps are highlighted in the images in B. Pink indicates cells following a linear regression; orange: cells sharing the same level of strain energy but displaying high variability in myosin content; green: cells displaying the same myosin content but high variability in strain energy. (B) Top panels: images of RPE-1 cells labeled for phospho-myosin (p-MLC). Bottom panels: corresponding traction stress maps. Image scale bar = 10 μm. Force scale color bar in Pa. The color code of the boxes refers to the points highlighted in the scatterplot in panel A. (C) Left panel: scatter plot of total myosin signal as a function of total F-actin signal in dual labeled cells. Right panel: scatter plot of the strain energy (pJ) as a function of total phospho-myosin/F-actin signal in dual labeled cells. The Pearson correlation coefficients and corresponding R^2 are indicated on the plots. The same color code as displayed in the Left panel was used to highlight strain energy values of each individual cell.

DISCUSSION

The implementation of an intermediate immunolabeling step in the standard TFM assay allowed us to evaluate the relationship between the traction force exerted by single epithelial RPE-1 cells onto their underlying substrate and the endogenous biochemical composition of their actomyosin network and adhesion machinery. Although the analyzed cells adopted a standardized shape on the dumbbell micropatterns, there were wide variations between cells in strain energies and signals from the cytoskeletal components, such that these heterogeneities helped identify relationships across the cell population between strain energy and the cytoskeletal components.

Hence, we identified vinculin content as a reliable predictor of force (Figure 2B), in agreement with the structural role of FAs as being the convergence point of all the traction forces produced in cells (Chang and Kumar, 2013). Previous studies, in which measurements were performed at the scale of individual focal

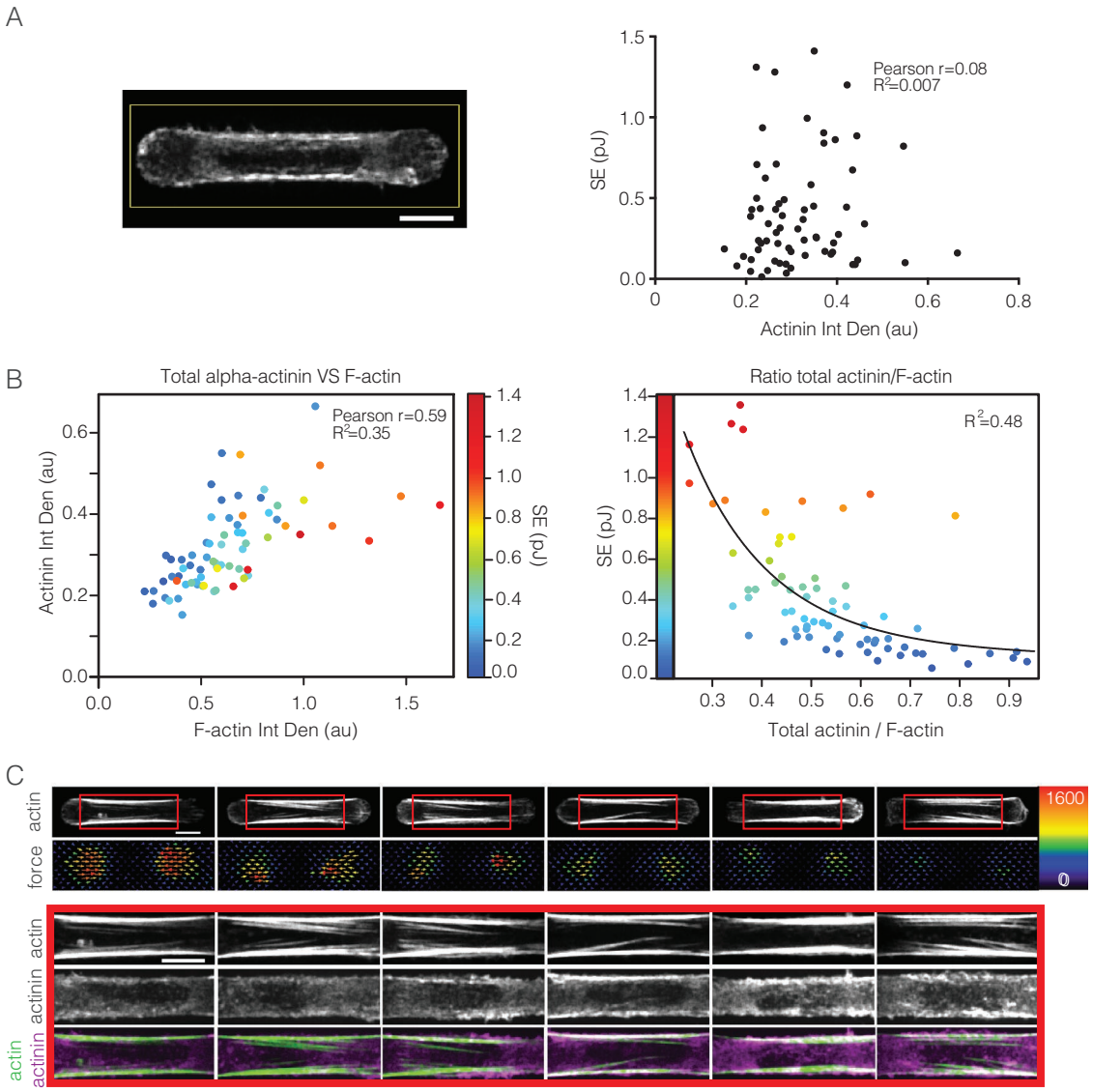

FIGURE 5: The relative amount of α-actinin per total actin filament sets the magnitude of force production. (A) Left panel: image of an RPE-1 cell depicting the area used for measurement of total α-actinin signal (yellow box). Image scale bar = 10 μm. Right panel: scatter plot of the strain energy (pJ) as a function of total α-actinin signal (au) in dual-labeled cells. The Pearson correlation coefficient and corresponding R^2 are indicated on top of the plot. (B) Left panel: scatter plot of the total α-actinin signal as a function of total F-actin signal (au). The Pearson correlation coefficient and corresponding R^2 are indicated on top of the plot. Dots were color coded according to the strain energy values measured for each individual cell. Right panel: scatter plot of the strain energy (pJ) as a function of total actinin/F-actin ratio. The R^2 corresponding to an exponential decay fit is indicated on top of the plot. The same color code as displayed in the Left panel was used to highlight strain energy values of each individual cell. (C) Top panels: selected images of RPE-1 cells labeled for F-actin (phalloidin) displaying an increase in their α-actinin total content and images of the corresponding traction stress maps. Image scale bar = 10 μm. Force color scale bar in Pa. Bottom panels: zoom-in images corresponding to the red insets above displaying actin, α-actinin 4 and overlays of both labels in the same cells. Image scale bar = 10 μm.

adhesions, reported different if not opposing views on the relationship between FA composition/size and force, depending on the cellular context of the study (Balaban *et al.*, 2001; Tan *et al.*, 2003; Stricker *et al.*, 2011; Trichet *et al.*, 2012; Oakes and Gardel, 2014). In particular, a positive correlation between individual FA size and local traction force was observed only during the initial stages of FA assembly in migrating cells, but was no longer valid for mature FA (Stricker *et al.*, 2011). Under our conditions, cells were not migrating, and measurements were performed at the entire cell-level several hours after cell spreading on micropatterns, showing that this positive correlation between FA size and force still holds in mature FAs. In addition, we observed that FAs formed a dense peripheral beltlike structure. The length and vinculin staining intensity of this belt, but not its thickness, were greater with higher traction force, to the extent that this belt appeared as a continuous structure above the circumference of each of the two circular parts of the micropattern (Figure 2C). This result suggested that the shape and size of this peripheral belt reflected the balance between outward growth by tensional forces (Mack *et al.*, 2004) and inward translocation by retrograde

flow (Zamir *et al.*, 2000; Alexandrova *et al.*, 2008). This balance may contribute to the regulation of the maximal force produced by the cell.

Both actin filament and phospho-myosin content displayed positive correlations with traction forces exerted by cells (Figures 3A and 4A), in agreement with the main role played by myosin pulling on actin filaments to generate intracellular contractility (Thoresen *et al.*, 2011; Reymann *et al.*, 2012; Stachowiak *et al.*, 2012). However, their individual contents only partially predicted traction-force magnitude and the production of high traction forces appeared to require both phospho-myosin and F-actin in an optimum ratio (Figure 4C). This is consistent with the complex functional roles of myosin pulling on actin filaments in generating intracellular force (Thoresen *et al.*, 2011; Reymann *et al.*, 2012; Stachowiak *et al.*, 2012) and in cross-linking and disassembling actin filaments (Haviv *et al.*, 2008; Wilson *et al.*, 2010; Reymann *et al.*, 2012; Stachowiak *et al.*, 2014; Matsuda *et al.*, 2018).

In contrast, α-actinin content alone was unable to predict traction-force magnitude (Figure 5A), even though it plays a key role in the regulation of forces (Oakes *et al.*, 2012; Senger *et al.*, 2019). However, the α-actinin/phospho-myosin and α-actinin/F-actin ratios were negatively correlated with the magnitude of traction forces (Supplemental Figure 3B and Figure 5B). This last result appeared to differ from the bell-shaped curve relationship between contractile force and α-actinin/actin ratios described for actin networks in vitro (Bendix *et al.*, 2008; Alvarado *et al.*, 2013; Ennomani *et al.*, 2016). One hypothesis is that there was redundancy between α-actinin and other cross-linkers, such as fascin, which plays a critical role in SF organization and traction force generation (Elkhatib *et al.*, 2014), and those crosslinkers functioned in the absence of α-actinin. Another possible explanation is that myosin, through its cross-linking activity (Laevsky and Knecht, 2003; Choi *et al.*, 2008), could stabilize the actin network and maintain the connectivity of the network in the presence of very low α-actinin levels. We also cannot exclude the possibility that cells displaying very low amount of α-actinin per actin filament and exerting weak traction forces were not included in the analysis because they failed to spread entirely on the micropattern.

Our results further indicated that actin filament content in the entire cell was as good as a predictor of traction-force magnitude as the F-actin content in stress fibers (Figure 3, A and B). Also, the cortical meshwork represented about half of the total actin filament signal intensity in this cell line. This suggested that stress fibers and the cortical meshwork contributed equally to traction-force generation. In agreement with this conclusion, FAs were found not only at the anchorage points of prominent stress fibers, but also all around the adhesive edge of the micropattern, where no prominent bundles were observed (Figure 2, A and C), indicating that the cortical meshwork of actin filaments was actively pulling on the substrate via these anchorage points, as suggested elsewhere (Kumar *et al.*, 2019; Vignaud *et al.*, 2021).

In conclusion, our method, in addition to being precise and unbiased by the topography of the substrate, can be used to evaluate the relationship between traction forces and endogenous proteins in different cellular contexts. Although the use of standard fluorophores for marking proteins, beads, and micropatterns limited the characterization to two proteins at a time, our method has the potential to expand the repertoire of proteins evaluated in a single cell by application of spectral multiplexed imaging with DNA-PAINT technology (Jungmann *et al.*, 2014; Wang *et al.*, 2017; Wade *et al.*, 2019).

MATERIALS AND METHODS

Photomask design

The photomask was designed using CleWin software and then manufactured by TOPPAN Photomasks. The dumbbell-shaped micropattern (Figure 1C) was designed as previously described in (Vignaud *et al.*, 2021). The micropattern consisted of two disks of diameter 12 μm separated by a center-to-center distance of 47 μm. The disks were connected by a 1 μm–wide line guiding the cells during their spreading between the disks. The micropattern was oriented at 45° to the horizontal, thereby providing the greatest separation between adjacent micropatterns and preventing the beads' displacement from adjacent cells from being detected in the imaging field of view. Every third dumbbell micropattern was numbered (Figure 1C) in both horizontal and vertical directions for redundancy in finding cells.

Fiduciary marks were designed in addition to the dumbbells in order to retrieve the exact sample location during the different steps of the process including sample removal from the microscope stage. The camera field of view when a 60× objective was used was 113.6 × 113.6 μm. A single vertical and horizontal array of circles (diameter 113.6 μm, center–center distance 227.2 μm) intersecting at the center of the pattern field divided the sample into four quadrants. At the center of the pattern field, where the arrays of circles intersected, the letters A, B, C, D were placed as shown in Figure 1C. These arrays of circles and the letters were used for preliminary translation and rotation alignment on the microscope. On the four vertices of each region, with the dumbbell/letter/circle patterns in the center, a set of small symbols (+, o, □) of width and height 10 μm and line thickness 2 μm were used for the final manual rotation correction. When these were present at the vertices of the camera field of view, the gel was considered to be aligned, achieving a rotation error of less than 1°.

Preparation of micropatterned polyacrylamide gels

Patterned polyacrylamide hydrogels were prepared following the guidelines previously described in Vignaud *et al.* (2014). A quartz photomask was first cleaned for 3.5 min with oxygen plasma (AST product, 300 W) at 200 W. Micropatterns were then incubated with 0.1 mg/ml PLL-g-PEG (JenKem Technology ZL187P072) in 10 mM HEPES, pH 7.4, for 30 min. After dewetting, the mask was exposed under deep UV for 5 min. Next, micropatterns on the mask were incubated with a mix of 10 μg/ml fibronectin (#F1141, Sigma) and 20 μg/ml fibrinogen-Alexa-Fluor-647 conjugate (#F35200, Invitrogen) in 100 mM sodium bicarbonate buffer, pH 8.4, for 30 min. A mix of acrylamide (8%) and bis-acrylamide solution (0.264%; Sigma) corresponding to a theoretical Young modulus of 19.66 kPa was degassed for approximately 30 min, mixed with 0.2 μm PLL-PEG covalently coated fluorescent beads (Fluorosphere #F8810, Life Technologies), and sonicated before addition of APS and TEMED. A quantity of 25 μl of that solution was added on the micropatterned photomask, covered with a silanized coverslip (Silane, #M6514, Sigma), and allowed to polymerize for 25 min before being gently detached in the presence of sodium bicarbonate buffer. Micropatterns were stored overnight in sodium bicarbonate buffer at 4°C before cells were plated.

Cell culture

Human telomerase-immortalized retinal-pigmented epithelial cells (hTERT RPE-1 from ATCC® CRL-4000™) were grown in a humidified incubator at 37°C and under 5% CO_2 in DMEM/F12 medium supplemented with 10% fetal bovine serum and 1% Antibiotic-Antimycotic (Thermo Fisher Scientific). Cells were plated on patterned

polyacrylamide gels at approximately 15,000 cells/ml and left to spread for 3 to 4 h before imaging.

Imaging process for traction force microscopy assay

Traction force mapping and immunostainings were performed and imaged on a Nikon confocal spinning-disk system (Eclipse Ti-E) equipped with a CSUX1-A1 Yokogawa confocal head and an Evolve EMCCD camera from Gataca Systems. A 20× objective was used for initial placement of the sample on the field of view (PlanAPO 20×/0.75). At this magnification, a 3 × 3 array of the patterns fit within the imaging window. The sample was rotated to the correct orientation using the alignment marks next to the micropatterns. It was then translated using the numbering next to the patterns as a reference to get to the center of the pattern field, which contains the patterned letters A, B, C, and D (Figure 1C). The 60× oil objective was then used for acquisition following minor rotation and translation adjustments to get one of the letters within the field of view, with the alignment marks appearing at the four corners of the imaging window. The stage position of the chosen letter was recorded to be used as a reference when the system was realigned for imaging the sample at the different steps of the process.

Well-spread individual cells on the micropatterns were selected by manually scanning the gel and their positions were recorded, along with the fiduciary marks. Live cells, together with their micropatterns and the beads corresponding to the deformed gel configuration, were first imaged. Following sample removal from the stage top, cells were then prepermeabilized, fixed, and labeled using the antibodies of interest. The sample was then placed back on the stage top and moved to the reference position recorded earlier. A realignment to the reference letter chosen earlier at 20× was made and minor corrections were then performed at 60×. The cells were next imaged for the fluorescent components (10 *z* slices, 0.75-μm spacing), the beads, and the micropatterns. During the whole process, the temperature was maintained at 37°C and the gels were kept in a wet environment to avoid any changes in the gel mechanical properties.

To detach cells, the samples were left overnight in 10× TGS buffer (BIO-RAD, 161-0772), washed four times with phosphate-buffered saline (PBS), and then treated with TryplE reagent (Life Technologies, 12605-010) for 1 h at 37°C. The cells detached on pipetting vigorously onto the surface of the gel. After cell detachment, the gels were placed back on the stage top incubator and realigned and the positions were reimaged for the beads and micropatterns.

Fixation and labeling

For labeling phospho-myosin light chain (p-MLC), α-actinin, and vinculin, cells were prepermeabilized in 0.5% Triton X-100 in Cytoskeleton buffer, pH 6.1, for 10 s and then immediately fixed in 4% paraformaldehyde in Cytoskeleton buffer with 10% sucrose, pH 6.1, for 20 min at room temperature. The cells were washed twice in Cytoskeleton buffer to get rid of excess paraformaldehyde and the fluorescence was then quenched in 0.1-M ammonium chloride for 10 min and then washed thrice in PBS. A solution of 1% BSA and 10% FBS in PBS was used for blocking for 1 h at room temperature before the sample was incubated overnight at 4°C in a humid chamber with appropriate dilutions of primary antibodies in PBS, 1% BSA, and 0.1% Tween.

The following antibodies were used: anti-phospho-myosin light chain 2 (#3671, CST), anti-α-actinin (#05-384, Millipore), anti-α-actinin4 (19096-1-AP, Protein tech), anti-vinculin-clone hVIN-1(V9131, Sigma), anti-rabbit Alexa Fluor-488 (A21441, Molecular Probes), and anti-mouse Alexa Fluor-546 (A11003, Invitrogen). For the data set where actin alone was imaged, prepermeabilization was not performed. The cells were fixed, washed thrice in PBS, and labeled for F-actin using Phalloidin-FITC (#P5282, Sigma).

Image Processing

Analyses were performed using Matlab and ImageJ software. A maximum-intensity projection of the *z*-stacks of each set of fluorescently labeled cells was first created. The images were rotated by 45° to have the long axis of the cell horizontal in the image, cropped to 300 × 300 pixels with the cells in the center. The average signal intensity in a 50 × 50–pixel region at the top of the cropped image was calculated for background subtraction. The sum of the signal in all the pixels after the background was subtracted provided the relative measure of the total protein content in each cell. From all the cells imaged, only those with two well-established stress fibers, one on either side of the long axis of the cell, were chosen for quantification of the fluorescent signal and TFM analysis. To isolate the signal from the stress fibers, the images were processed in ImageJ. A segmented line of width 5 pixels (1.11 μm) was drawn over each of the two stress fibers present in each cell (red lines in Figure 3B). The signal intensity integrated under the line was obtained using the measure tool integrated density from ImageJ. The sum of the noise-subtracted signals from the two stress fibers of each cell was taken as a measure of the relative protein content in these structures.

Translation and rotation correction were performed using the normxcorr2 function in custom written functions. Translation correction was done using the peak in the normalized cross-correlation matrix (*C*) between the reference bead image (with force, Figure 1A) and the bead image to be corrected (relaxed configuration, Figure 1A). The normalized cross-correlation between the with-force image and the translation-corrected image ("translation corrected") rotated by 0.1° in both clockwise and counterclockwise directions was calculated. The direction with the highest value of *C* was chosen to be the direction of rotation (b). The rotation and calculation of *C*, correcting for translation at each step, was iteratively done, comparing the *C* for the *n*th iteration with that for the (*n* – 1)th iteration until the first iteration where *C* decreased. The angle of rotation was given by $(n-1)\times\pm0.1°$, depending on the direction of rotation. The final translation and rotation correction values were then propagated to the pattern and cell images. Similarly, translation and rotation correction were done for the image of the partially relaxed gel (Figure 1B) with respect to the with-force image and the correction was propagated to the images of the pattern and fluorescently labeled components. The code and functions are available upon request.

Measurement of cell traction forces with ImageJ

Data were analyzed with a set of macros in Fiji using the method previously described in Martiel *et al*. (2015). Displacement fields were obtained from fluorescent bead images before and after removal of cells by trypsin treatment. Bead images already corrected for rotation and translation as described earlier were paired and realigned with a macro that corrected with subpixel accuracy (template matching). Displacement fields were calculated by particle imaging velocimetry, which uses a normalized cross correlation–based method with an iterative scheme. Final vector-grid size was 1.55 × 1.55 μm. Erroneous vectors were discarded owing to their low correlation values and replaced with the mean value of the neighboring vectors. Fourier-transform traction cytometry was used to compute the traction force field, with a regularization parameter set to 3.2×10^{-10}. Force vectors located outside of the micropattern area were discarded for calculation of strain energy.

Data analysis

Vinculin quantification was performed using the Focal Adhesion Analysis Server (Berginski *et al.*, 2011; Wu *et al.*, 2012; https://faas.bme.unc.edu/) with default settings. We used two global parameters for the quantification: the total adhesion area per cell and the total adhesion signal, respectively the sum of the area and the signal of the detected adhesion structures.

Data plotting

For multiparametric representation, graphs have been produced using R (https://www.r-project.org/) and RStudio (https://rstudio.com/), relying on the use of the "plot3D" package (Karline Soetaert, plot3D: Tools for plotting 3-D and 2-D data, http://cran.r-project.org/web/packages/plot3D/vignettes/plot3D.pdf).

Statistical analysis

Statistical analysis and chart design were performed using Graphpad Prism 6 (www.graphpad.com) and R version 3.4.0 together with RStudio version 1.0.143.

ACKNOWLEDGMENTS

This work was supported by grants from the European Research Council (741773, AAA) awarded to L.B. and (771599, ICEBERG) awarded to M.T., and from the Agence Nationale de la Recherche ANR (ANR-14-CE11-0003-01, MaxForce) awarded to L.B. and M.T. We thank the live microscopy facility MuLife of IRIG/DBSCI, which received funding from GRAL, a program from the Chemistry Biology Health (CBH) Graduate School of University Grenoble Alpes (ANR-17-EURE-0003), for equipment access and use. We thank Matial Balland for helpful advice and comments during this work.

REFERENCES

Agarwal P, Zaidel-Bar R (2019). Principles of actomyosin regulation in vivo. Trends Cell Biol 29, 150–163.

Alexandrova AY, Arnold K, Schaub S, Vasiliev JM, Meister J-J, Bershadsky AD, Verkhovsky AB (2008). Comparative dynamics of retrograde actin flow and focal adhesions: formation of nascent adhesions triggers transition from fast to slow flow. PLoS One 3, e3234.

Alvarado J, Sheinman M, Sharma A, Mackintosh FC, Koenderink GH (2013). Molecular motors robustly drive active gels to a critically connected state. Nat Phys 9, 591–597.

Balaban NQ, Schwarz US, Riveline D, Goichberg P, Tzur G, Sabanay I, Mahalu D, Safran S, Bershadsky A, Addadi L, *et al.* (2001). Force and focal adhesion assembly: a close relationship studied using elastic micropatterned substrates. Nat Cell Biol 3, 466–472.

Banda OA, Sabanayagam CR, Slater JH (2019). Reference-free traction force microscopy platform fabricated via two-photon laser scanning lithography enables facile measurement of cell-generated forces. ACS Appl Mater Interfaces 11, 18233–18241.

Bendix PM, Koenderink GH, Cuvelier D, Dogic Z, Koeleman BN, Brieher WM, Field CM, Mahadevan L, Weitz DA (2008). A quantitative analysis of contractility in active cytoskeletal protein networks. Biophys J 94, 3126–3136.

Beningo KA, Dembo M, Kaverina I, Small JV, Wang YL (2001). Nascent focal adhesions are responsible for the generation of strong propulsive forces in migrating fibroblasts. J Cell Biol 153, 881–888.

Bergert M, Lendenmann T, Zündel M, Ehret AE, Panozzo D, Richner P, Kim DK, Kress SJP, Norris DJ, Sorkine-Hornung O, *et al.* (2016). Confocal reference free traction force microscopy. Nat Commun 7, 12814.

Berginski ME, Vitriol EA, Hahn KM, Gomez SM (2011). High-resolution quantification of focal adhesion spatiotemporal dynamics in living cells. PLoS One 6, e22025.

Biais N, Higashi D, So M, Ladoux B (2012). Techniques to measure pilus retraction forces. Methods Mol Biol 799, 197–216.

Califano JP, Reinhart-King CA (2010). Substrate stiffness and cell area predict cellular traction stresses in single cells and cells in contact. Cell Mol Bioeng 3, 68–75.

Chang C, Kumar S (2013). Vinculin tension distributions of individual stress fibers within cell–matrix adhesions. J Cell Sci 126, 3021–3030.

Choi CK, Vicente-Manzanares M, Zareno J, Whitmore LA, Mogilner A, Horwitz AR (2008). Actin and α-actinin orchestrate the assembly and maturation of nascent adhesions in a myosin II motor-independent manner. Nat Cell Biol 10, 1039–1050.

Chrzanowska-wodnicka M, Burridge K (1996). Rho-stimulated contractility drives the formation of stress fibers and focal adhesions. J Cell Biol 133, 1403–1415.

Deguchi S, Ohashi T, Sato M (2005). Intracellular stress transmission through actin stress fiber network in adherent vascular cells. Mol Cell Biomech 2, 205–216.

Dembo M, Wang YL (1999). Stresses at the cell-to-substrate interface during locomotion of fibroblasts. Biophys J 76, 2307–2316.

DePasquale JA, Izzard CS (1987). Evidence for an actin-containing cytoplasmic precursor of the focal contact and the timing of incorporation of vinculin at the focal contact. J Cell Biol 105, 2803–2809.

Elkhatib N, Neu MB, Zensen C, Schmoller KM, Louvard D, Bausch AR, Betz T, Vignjevic DM (2014). Fascin plays a role in stress fiber organization and focal adhesion disassembly. Curr Biol 24, 1492–1499.

Elosegui-Artola A, Oria R, Chen Y, Kosmalska A, Pérez-González C, Castro N, Zhu C, Trepat X, Roca-Cusachs P (2016). Mechanical regulation of a molecular clutch defines force transmission and transduction in response to matrix rigidity. Nat Cell Biol 18, 540–548.

Ennomani H, Letort G, Guérin C, Martiel J-L, Cao W, Nédélec F, De LaCruz EM, Théry M, Blanchoin L (2016). Architecture and connectivity govern actin network contractility. Curr Biol 26, 616–626.

Geiger B, Bershadsky A, Pankov R, Yamada KM (2001). Transmembrane extracellular matrix–cytoskeleton crosstalk. Nat Rev Mol Cell Biol 2, 793–805.

Ghagre A, Amini A, Srivastava LK, Tirgar P, Khavari A, Koushki N, Ehrlicher A (2021). Pattern-based contractility screening, a reference-free alternative to traction force microscopy methodology. ACS Appl Mater Interfaces, doi: 10.1021/acsami.1c02987.

Goffin JM, Pittet P, Csucs G, Lussi JW, Meister J-J, Hinz B (2006). Focal adhesion size controls tension-dependent recruitment of alpha-smooth muscle actin to stress fibers. J Cell Biol 172, 259–268.

Grashoff C, Hoffman BD, Brenner MD, Zhou R, Parsons M, Yang MT, McLean MA, Sligar SG, Chen CS, Ha T, *et al.* (2010). Measuring mechanical tension across vinculin reveals regulation of focal adhesion dynamics. Nature 466, 263–266.

Griffin BP, Largaespada CJ, Rinaldi NA, Lemmon CA (2019). A novel method for quantifying traction forces on hexagonal micropatterned protein features on deformable poly-dimethyl siloxane sheets. MethodsX 6, 1343–1352.

Haviv L, Gillo D, Backouche F, Bernheim-Groswasser A (2008). A cytoskeletal demolition worker: myosin II acts as an actin depolymerization agent. J Mol Biol 375, 325–330.

Heisenberg C-P, Bellaïche Y (2013). Forces in tissue morphogenesis and patterning. Cell 153, 948–962.

Jungmann R, Avendaño MS, Woehrstein JB, Dai M, Shih WM, Yin P (2014). Multiplexed 3D cellular super-resolution imaging with DNA-PAINT and Exchange-PAINT. Nat Methods 11, 313–318.

Katoh K, Kano Y, Masuda M, Onishi H (1998). Isolation and contraction of the stress fiber. Mol Biol Cell 9, 1919–1938.

Kilian Ka, Bugarija B, Lahn BT, Mrksich M (2010). Geometric cues for directing the differentiation of mesenchymal stem cells. Proc Natl Acad Sci USA 107, 4872–4877.

Koenderink GH, Paluch EK (2018). Architecture shapes contractility in actomyosin networks. Curr Opin Cell Biol 50, 79–85.

Kraning-Rush CM, Carey SP, Califano JP, Smith BN, Reinhart-King CA (2011). The role of the cytoskeleton in cellular force generation in 2D and 3D environments. Phys Biol 8, 15009.

Kumar A, Shutova MS, Tanaka K, Iwamoto DV, Calderwood DA, Svitkina TM, Schwartz MA (2019). Filamin A mediates isotropic distribution of applied force across the actin network. J Cell Biol 218, 2481–2491.

Kurzawa L, Vianay B, Senger F, Vignaud T, Blanchoin L, Théry M (2017). Dissipation of contractile forces: the missing piece in cell mechanics. Mol Biol Cell 28, 1825–1832.

Laevsky G, Knecht DA (2003). Cross-linking of actin filaments by myosin II is a major contributor to cortical integrity and cell motility in restrictive environments. J Cell Sci 116, 3761–3770.

Langanger G, Moeremans M, Daneels G, Sobieszek A, De Brabander M, De Mey J (1986). The molecular organization of myosin in stress fibers of cultured cells. J Cell Biol 102, 200–209.

Lazarides E, Burridge K (1975). Alpha-actinin: immunofluorescent localization of a muscle structural protein in nonmuscle cells. Cell 6, 289–298.

Leal-Egaña A, Letort G, Martiel J-L, Christ A, Vignaud T, Roelants C, Filhol O, Théry M (2017). The size–speed–force relationship governs migratory cell response to tumorigenic factors. Mol Biol Cell 28, 1612–1621.
Linsmeier I, Banerjee S, Oakes PW, Jung W, Kim T, Murrell MP (2016). Disordered actomyosin networks are sufficient to produce cooperative and telescopic contractility. Nat Commun 7, 1–9.
Lo CM, Wang HB, Dembo M, Wang YL (2000). Cell movement is guided by the rigidity of the substrate. Biophys J 79, 144–152.
Luo W, Yu C, Lieu ZZ, Allard J, Mogilner A, Sheetz MP, Bershadsky AD (2013). Analysis of the local organization and dynamics of cellular actin networks. J Cell Biol 202, 1057–1073.
Mack PJ, Kaazempur-Mofrad MR, Karcher H, Lee RT, Kamm RD (2004). Force-induced focal adhesion translocation: effects of force amplitude and frequency. Am J Physiol Cell Physiol 287, C954-62.
Maiuri P, Rupprecht JF, Wieser S, Ruprecht V, Bénichou O, Carpi N, Coppey M, De Beco S, Gov N, Heisenberg CP, *et al*. (2015). Actin flows mediate a universal coupling between cell speed and cell persistence. Cell 161, 374–386.
Martiel JL, Leal A, Kurzawa L, Balland M, Wang I, Vignaud T, Tseng Q, Théry M (2015). Measurement of cell traction forces with ImageJ. Methods Cell Biol 125, 269–287.
Matsuda K, Kobayashi T, Sugawa M, Koiso Y, Toyoshima YY, Yajima J (2018). Myosin-driven fragmentation of actin filaments triggers contraction of a disordered actin network. BioRxiv, doi: https://doi.org/10.1101/332684.
McBeath R, Pirone DM, Nelson CM, Bhadriraju K, Chen CS (2004). Cell shape, cytoskeletal tension, and RhoA regulate stem cell lineage commitment. Dev Cell 6, 483–495.
Möhl C, Kirchgessner N, Schäfer C, Hoffmann B, Merkel R (2012). Quantitative mapping of averaged focal adhesion dynamics in migrating cells by shape normalization. J Cell Sci 125, 155–165.
Murrell M, Oakes PW, Lenz M, Gardel ML (2015). Forcing cells into shape: the mechanics of actomyosin contractility. Nat Rev Mol Cell Biol 16, 486–498.
Naumanen P, Lappalainen P, Hotulainen P (2008). Mechanisms of actin stress fibre assembly. J Microsc 231, 446–454.
Oakes PW, Banerjee S, Marchetti MC, Gardel ML (2014). Geometry regulates traction stresses in adherent cells. Biophys J 107, 825–833.
Oakes PW, Beckham Y, Stricker J, Gardel ML (2012). Tension is required but not sufficient for focal adhesion maturation without a stress fiber template. J Cell Biol 196, 363–374.
Oakes PW, Gardel ML (2014). Stressing the limits of focal adhesion mechanosensitivity. Curr Opin Cell Biol 30, 68–73.
Plotnikov SV, Pasapera AM, Sabass B, Waterman CM (2012). Force fluctuations within focal adhesions mediate ECM-rigidity sensing to guide directed cell migration. Cell 151, 1513–1527.
Pushkarsky I, Tseng P, Black D, France B, Warfe L, Koziol-White CJ, Jester WF Jr, Trinh RK, Lin J, Scumpia PO, *et al*. (2018). Elastomeric sensor surfaces for high-throughput single-cell force cytometry. Nat Biomed Eng 2, 124–137.
Rape AD, Guo W-H, Wang Y-L (2011). The regulation of traction force in relation to cell shape and focal adhesions. Biomaterials 32, 2043–2051.
Reinhart-King CA, Dembo M, Hammer DA (2005). The dynamics and mechanics of endothelial cell spreading. Biophys J 89, 676–689.
Reymann A-C, Boujemaa-Paterski R, Martiel J-L, Guerin C, Cao W, Chin HF, De La Cruz EM, Thery M, Blanchoin L (2012). Actin network architecture can determine myosin motor activity. Science (80-) 336, 1310–1314.
Roca-Cusachs P, Conte V, Trepat X (2017). Quantifying forces in cell biology. Nat Cell Biol 19, 742–751.
Sedzinski J, Biro M, Oswald A, Tinevez JY, Salbreux G, Paluch E (2011). Polar actomyosin contractility destabilizes the position of the cytokinetic furrow. Nature 476, 462–468.
Senger F, Pitaval A, Ennomani H, Kurzawa L, Blanchoin L, Théry M (2019). Spatial integration of mechanical forces by α-actinin establishes actin network symmetry. J Cell Sci 132, 22.
Stachowiak MR, McCall PM, Thoresen T, Balcioglu HE, Kasiewicz L, Gardel ML, O'Shaughnessy B (2012). Self-organization of myosin II in reconstituted actomyosin bundles. Biophys J 103, 1265–1274.
Stachowiak MR, Smith MA, Blankman E, Chapin LM, Balcioglu HE, Wang S, Beckerle MC, O'Shaughnessy B (2014). A mechanical–biochemical feedback loop regulates remodeling in the actin cytoskeleton. Proc Natl Acad Sci USA 111, 17528–17533.
Stricker J, Aratyn-Schaus Y, Oakes PW, Gardel ML (2011). Spatiotemporal constraints on the force-dependent growth of focal adhesions. Biophys J 100, 2883–2893.
Tan JL, Tien J, Pirone DM, Gray DS, Bhadriraju K, Chen CS (2003). Cells lying on a bed of microneedles: an approach to isolate mechanical force. Proc Natl Acad Sci USA 100, 1484–1489.
Thoresen T, Lenz M, Gardel ML (2011). Reconstitution of contractile actomyosin bundles. Biophys J 100, 2698–2705.
Trichet L, Le Digabel J, Hawkins RJ, Vedula SRK, Gupta M, Ribrault C, Hersen P, Voituriez R, Ladoux B (2012). Evidence of a large-scale mechanosensing mechanism for cellular adaptation to substrate stiffness. Proc Natl Acad Sci USA 109, 6933–6938.
Tseng Q, Wang I, Duchemin-Pelletier E, Azioune A, Carpi N, Gao J, Filhol O, Piel M, Théry M, Balland M (2011). A new micropatterning method of soft substrates reveals that different tumorigenic signals can promote or reduce cell contraction levels. Lab Chip 11, 2231–2240.
Vignaud T, Copos C, Leterrier C, Toro-Nahuelpan M, Tseng Q, Mahamid J, Blanchoin L, Mogilner A, Théry M, Kurzawa L (2021). Stress fibres are embedded in a contractile cortical network. Nat Mater 20, 410–420.
Vignaud T, Ennomani H, Théry M (2014). Polyacrylamide hydrogel micropatterning. Methods Cell Biol 120, 93–116.
Wade OK*et al*. (2019). 124-color super-resolution imaging by engineering DNA-PAINT blinking kinetics. Nano Lett 19, 2641–2646.
Wang X, Ha T (2013). Defining single molecular forces required to activate integrin and notch signaling. Science 340, 991–994.
Wang Y*et al*. (2017). Rapid sequential in situ multiplexing with DNA exchange imaging in neuronal cells and tissues. Nano Lett 17, 6131–6139.
Wilson CA, Tsuchida MA, Allen GM, Barnhart EL, Applegate KT, Yam PT, Ji L, Keren K, Danuser G, Theriot JA (2010). Myosin II contributes to cell-scale actin network treadmilling through network disassembly. Nature 465, 373–377.
Wu C, Asokan SB, Berginski ME, Haynes EM, Sharpless NE, Griffith JD, Gomez SM, Bear JE (2012). Arp2/3 is critical for lamellipodia and response to extracellular matrix cues but is dispensable for chemotaxis. Cell 148, 973–987.
Xu J, Wirtz D, Pollard TD (1998). Dynamic cross-linking by alpha-actinin determines the mechanical properties of actin filament networks. J Biol Chem 273, 9570–9576.
Zamir E, Katz M, Posen Y, Erez N, Yamada KM, Katz BZ, Lin S, Lin DC, Bershadsky A, Kam Z, *et al*. (2000). Dynamics and segregation of cell–matrix adhesions in cultured fibroblasts. Nat Cell Biol 2, 191–196.